A&A 654, A140 (2021)
https://doi.org/10.1051/0004-6361/202141629

Astronomy & Astrophysics

Sr and Ba abundances: Comparing machine-learning with star-by-star analyses

High-resolution re-analysis of suspected LAMOST barium stars

D. Karinkuzhi[1,2], S. Van Eck[2], A. Jorissen[2], A. Escorza[3], S. Shetye[2], T. Merle[2], L. Siess[2], S. Goriely[2], and H. Van Winckel[4]

[1] Department of Physics, Indian Institute of Science, Bangalore 560012, India
e-mail: drisyadev@gmail.com
[2] Institut d'Astronomie et d'Astrophysique, Université Libre de Bruxelles C.P. 226, Boulevard du Triomphe, 1050 Bruxelles, Belgium
e-mail: svaneck@astro.ulb.ac.be; ajorisse@astro.ulb.ac.be
[3] European Southern Observatory, Alonso de Córdova 3107, Vitacura, Casilla 19001, Santiago de Chile, Chile
[4] Instituut voor Sterrenkunde, KULeuven, Celestijnenlaan 200D, 3001 Leuven, Belgium

Received 24 June 2021 / Accepted 9 July 2021

ABSTRACT

Context. A new large sample of 895 s-process-rich candidates out of 454 180 giant stars surveyed by LAMOST at a low spectral resolution ($R \sim 1800$) has been reported by Norfolk et al. (2019, MNRAS, 490, 2219; hereafter N19).
Aims. This study is aimed at confirming the s-process enrichment at the higher resolution ($R \sim 86\,000$) offered by the HERMES-*Mercator* spectrograph for the 15 brightest targets of the N19 sample, which consists of 13 Sr-only stars and two Ba-only stars (designating stars with only the Sr or only Ba lines strengthened).
Methods. Abundances were derived for elements Li, C (including the $^{12}C/^{13}C$ isotopic ratio), N, O, Na, Mg, Fe, Rb, Sr, Y, Zr, Nb, Ba, La, and Ce, using the TURBOSPECTRUM radiative transfer LTE code with MARCS model atmospheres. Binarity has been tested by comparing the *Gaia* DR2 radial velocity (epoch 2015.5) with the HERMES velocity obtained 1600–1800 days (about 4.5 yr) later.
Results. Among the 15 programme stars, 4 show no s-process overabundances ([X/Fe] < 0.2 dex), 8 show mild s-process overabundances (at least three heavy elements with 0.2 < [X/Fe] < 0.8), and 3 have strong overabundances (at least three heavy elements with [X/Fe] ≥ 0.8). Among the 13 stars classified as Sr-only by the previous investigation, 4 have no s-process overabundances, 8 are mild barium stars, and 1 is a strong barium star. The two Ba-only stars turn out to be both strong barium stars. Especially noteworthy is the fact that these two are actually dwarf barium stars. Two among the three strong barium stars show clear evidence in support of their binary character, as expected for objects produced through mass-transfer. The results for the no s-process and mild barium stars are more surprising; namely, among the no-s stars, there are two binaries out of four, whereas only one out the eight diagnosed mild barium stars shows a clear signature of radial-velocity variations.
Conclusions. Blending effects and saturated lines have to be considered very carefully when using machine-learning techniques, especially when applied to low-resolution spectra. Among the Sr-only stars from the previous study sample, about 60% (8/13) of them can be expected to be true mild barium stars and about 8% to be strong barium stars; this fraction is likely close to 100% for the N19 Ba-only stars (2/2). Therefore, we recommend to limit the sample to N19 Ba-only stars when one needs an unpolluted sample of mass-transfer (i.e., extrinsic) objects.

Key words. stars: abundances – stars: late-type – stars: low-mass

1. Introduction

Barium (Ba) stars or Ba II stars, as they were originally named, are G- and K-type giants with strong absorption lines of slow-neutron-capture (s)-process elements in their spectra and with enhanced carbon-bearing molecular bands. They were first identified as appearing chemically peculiar by Bidelman & Keenan (1951), who discussed their distinctive spectroscopic characteristics and stressed the extraordinary strength of the resonance line of ionised barium at 4554 Å. The resulting overabundance of barium and other s-process elements on the surface of these stars could not be explained from an evolutionary point of view because the s-process of nucleosynthesis takes place in the interiors of asymptotic giant branch (AGB) stars, whereas Ba stars are instead dwarf, subgiant, red giant branch (RGB), or red-clump stars (e.g. Jorissen et al. 2019; Escorza et al. 2019). Barium stars are understood to originate from a binary evolution channel (McClure 1983). According to this formation scenario, the carbon and the s-process elements were transferred to the current primary from a more evolved companion when the latter was in its AGB phase. Galactic chemical evolution provides an alternative explanation for mild barium stars (with [Ba/Fe] ∼ 0.2−0.3 dex), which represent the upper [Ba/Fe] tail of the Galactic ([Ba/Fe],[Fe/H]) trend (e.g. Edvardsson et al. 1993; Tautvaišienė et al. 2021).

Since recently, the largest homogeneous sample of barium stars had been collected in the course of the Michigan Spectral Sky Survey, with 205 new discovered barium stars (MacConnell et al. 1972). Mainly on the basis of this sample, Lü et al. (1983) then built their catalogue with 221 entries, followed by an

updated version with 389 stars (Lü 1991). However, a substantial fraction of them are probably not barium stars (especially those classified with a Ba index[1] ≤1; e.g. Smiljanic et al. 2007).

More recently, large-field spectroscopic surveys like LAMOST (Wu et al. 2011; Bai et al. 2016), involving low-resolution spectroscopy, have permitted a sizable potential increase in the number of known stars with enhanced s-process elements. For instance, Norfolk et al. (2019, hereafter N19) reported 859 candidates (out of 454 180 giants studied) that were classified as either Sr-only, Ba-only, or Ba- and Sr-strong. This classification was based on the comparison between the strengths of the most conspicuous Sr II (4077 and 4215 Å) and Ba II lines (4554, 4934, and 6496 Å) in template and target stars, using the machine-learning technique known as *The Cannon* (Ness et al. 2015). There are, however, several caveats (as we discuss below) with this approach, which call for an a posteriori verification of the s-process enhancement from high-resolution spectra. Only one star was subject to such a check by N19.

The purpose of this paper is to perform such a verification on a larger sample of 15 stars. The motivation thereof is the very low resolution of LAMOST spectra ($R \sim 1800$), combined with the fact that the above-mentioned lines of Sr II and Ba II are known to show a positive luminosity effect (i.e. strengthening of the line due to low gravity rather than overabundance; Gray et al. 2009). Moreover, some of those lines are blended (e.g. Sr II 4215.5 Å by CN lines) and are often saturated, in which case they become poor diagnostics for measuring abundances.

Recently, the Sr abundance in Carbon-Enhanced Metal-Poor (CEMP) stars has gained a lot of attention since some studies (Hansen et al. 2016, 2019) have found that the Sr/Ba ratio can be used to separate CEMP stars into their sub-groups (CEMP-no, CEMP-s, and CEMP-rs) and to identify their progenitors since this ratio depends on the nucleosynthetic sites.

Large-field spectroscopic surveys have provided spectra for millions of stars and machine-learning techniques are widely used to measure abundances of the elements. Our current analysis is aimed at discussing the difficulties in measuring the abundances of Sr and Ba, especially when using machine-learning techniques on low-resolution spectra.

In this paper, we present a detailed high-resolution spectroscopic analysis of the brightest s-process-rich candidates of N19 in order (i) to check for possible misclassification as (mild) barium stars; (ii) to understand the origin of the variations in their individual elemental abundance pattern and thereby understand the origin of these peculiar abundances; and (iii) to evaluate the power of machine-learning techniques for abundance determination from low-resolution spectra.

This paper is organised as follows. Section 2 describes the selection of the sample. Section 3 discusses the method used for deriving the atmospheric parameters. Section 4 presents the abundance analysis. Section 5 compares N19 classification with ours, whereas Sect. 6 presents comments about individual stars. Section 7 discusses the possible origin of the peculiarities of the different identified classes and, finally, Sect. 8 discusses the efficiency with which *The Cannon* machine-learning method has been able to correctly flag s-process-enriched stars from low-resolution spectra. Our conclusions are presented in Sect. 9.

[1] The Ba index (spanning the range 1–5, later extended to 0–5) has been defined by Warner (1965) based on a visual inspection of the strength of the Ba II 4554 Å line, the index 5 corresponding to the strongest line strength.

2. Sample selection

Our analysis focuses on the brightest among the stars from N19 tagged as 'Sr only' or 'Ba only' candidates (designating stars with either only the Sr or only Ba lines strengthened, respectively; see Sects. 4.3 and 4.4), visible from the Roque de los Muchachos Observatory in La Palma, Canary Islands (Spain). They are listed in Table 1, along with the N19 classification. They were observed with the high-resolution HERMES spectrograph (Raskin et al. 2011) mounted on the 1.2 m *Mercator* telescope. The spectra cover the spectral range 3900–9000 Å with a resolution of 86 000. The signal-to-noise ratio (S/N) of the HERMES spectra around 5000 Å is listed in Table 1.

3. Derivation of atmospheric parameters

The atmospheric parameters of the programme stars were derived following the same method as outlined by Karinkuzhi et al. (2018). We used the BACCHUS (Brussels Automatic Code for Characterizing High accUracy Spectra) tool in a semi-automated mode (Masseron et al. 2016). BACCHUS combines interpolated MARCS model atmospheres (Gustafsson et al. 2008) with the 1D local-thermodynamical-equilibrium (LTE) spectrum-synthesis code TURBOSPECTRUM (Alvarez & Plez 1998; Plez 2012). We manually selected Fe I and Fe II lines so as to select blending-free lines for BACCHUS to derive the stellar parameters ($T_{\rm eff}$, [Fe/H], $\log g$, microturbulence velocity ξ as well as rotational velocity). The code includes on the fly spectrum synthesis, local continuum normalization, estimation of local S/N, and automatic line masking. It computes abundances using equivalent widths or spectral synthesis, allowing us to check for excitation and ionization equilibria, and thereby constraining $T_{\rm eff}$ and $\log g$. The microturbulent velocity ξ is calculated by ensuring consistency between Fe abundances derived from lines of various reduced equivalent widths.

4. Abundance analysis

Abundances were derived by comparing observed and synthetic spectra generated with the TURBOSPECTRUM code. The solar abundances were taken from Asplund et al. (2009). We used the line lists assembled in the framework of the *Gaia*-ESO survey (Heiter et al. 2015; Heiter 2020) and presented in Karinkuzhi et al. (2018, 2021); hence, we do not list them here. The abundances were derived under the LTE assumption, but a posteriori NLTE corrections have been added whenever available, as we discuss below. In Tables A.1 and A.2, we present all the abundances derived from our target stars. In the following, we comment on individual elemental abundances.

4.1. Li

The Li abundance has been derived from the Li I 6707 Å line. We could measure the Li abundance in only two stars, TYC 3144−1906−1 and BD −07°402 with $\log \epsilon$(Li) ≈ 0.6 and 1.3 dex, respectively (Table A.2). These values are in accordance with the Li abundance of 1.0 dex, as predicted in RGB stars after the first dredge up (e.g. Jorissen et al. 2020, and references therein)

4.2. C, N, and O

We derived oxygen abundances from the [O I] line at 6300.303 Å except for TYC 591−1090−1 where the O I resonance triplet at 7774 Å is used instead. A non-LTE correction

Table 1. Programme stars and adopted atmospheric parameters.

Name	$T_{\rm eff}$ (K)	$\log g$ (cm s^{-2})	[Fe/H] (dex)	ξ (km s^{-1})	S/N	Class
			No s-process enrichment			
HD 7863	4637 ± 64	2.29 ± 0.40	−0.07 ± 0.05	1.26 ± 0.10	68	No
	4561 ± 6	2.37 ± 0.01	0.13 ± 0.01	2	–	Sr only
HIP 69788	5127 ± 11	3.90 ± 0.14	−0.04 ± 0.04	0.61 ± 0.10	75	No
	4913 ± 10	3.04 ± 0.02	−0.34 ± 0.01	2	–	Sr-only
TYC 3144−1906−1	4136 ± 64	1.89 ± 0.50	−0.13 ± 0.10	1.37 ± 0.04	48	No (Li)
	4232 ± 8	1.87 ± 0.02	0.15 ± 0.01	2	–	Sr only
TYC 4684−2242−1	4651 ± 20	2.70 ± 0.14	−0.05 ± 0.07	1.15 ± 0.05	54	No
	4652 ± 12	2.71 ± 0.03	0.05 ±0.02	2	–	Sr only
			Mild s-process enrichment			
BD −07° 402	4654 ± 6	2.62 ± 0.19	−0.11 ± 0.05	1.22 ± 0.10	61	Mild (Li-rich)
	4688 ± 9	2.58 ± 0.02	0.11 ± 0.01	2	–	Sr only
BD +44° 575	4175 ± 6	1.50 ± 0.19	−0.45 ± 0.05	1.60 ± 0.10	76	Mild
	4202 ± 12	1.59 ± 0.03	−0.11 ± 0.02	2	–	Sr only
TYC 22−155−1	4704 ± 9	3.10 ± 0.32	−0.20 ± 0.10	1.04 ± 0.05	47	Mild
	4629 ± 11	2.72 ± 0.03	−0.22 ± 0.01	2	–	Sr only
TYC 2913−1375−1	4757 ± 69	2.00 ± 0.30	−0.61 ± 0.11	1.45 ± 0.05	32	Mild
	4791± 15	2.41± 0.04	−0.37 ± 0.02	2	–	Sr only
TYC 3305−571−1	4816 ± 3	2.76 ± 0.16	−0.05 ± 0.08	1.31 ± 0.04	49	Mild
	4798 ± 8	2.62 ± 0.02	0.18 ± 0.01	2	–	Sr only
TYC 752−1944−1	5069 ± 25	2.94 ± 0.05	−0.08 ± 0.08	1.33 ± 0.04	61	Mild
	4967 ± 11	2.79 ± 0.03	0.02 ± 0.01	2	–	Sr only
TYC 4837−925−1	4679 ± 34	2.16 ± 0.29	−0.27 ± 0.07	1.30 ± 0.04	44	Mild
	4739 ± 14	2.46 ± 0.04	0.02 ± 0.02	2	–	Sr only
TYC 3423−696−1	5042 ± 64	3.66 ± 0.30	0.02 ± 0.08	0.96 ± 0.04	55	Mild
	5014 ± 17	3.59 ± 0.03	0.22 ± 0.02	2	–	Sr only
			Strong s-process enrichment			
TYC 2250−1047−1	5335 ± 25	3.71 ± 0.18	−0.55 ± 0.12	1.45 ± 0.05	32	Strong
	5097 ± 23	3.25 ± 0.03	−0.68 ± 0.03	2	–	Ba only
TYC 2955−408−1	4716 ± 64	2.49 ± 0.3	−0.39 ± 0.08	1.25 ± 0.04	61	Strong
	4724 ± 10	2.39 ± 0.03	−0.21 ± 0.01	2	–	Sr only
TYC 591−1090−1	5267 ± 36	3.68 ± 0.50	−0.30 ± 0.12	1.18 ± 0.06	28	Strong
	5106 ± 13	3.33 ± 0.02	−0.29 ± 0.01	2	–	Ba only

Notes. ξ is the microturbulence velocity. The column 'S/N' gives the signal-to-noise ratio (around 5000 Å) of the HERMES spectrum used for the abundance analysis. The column "class" indicates classification either from our study (first line), or from N19 on the second line. For the criteria used to classify stars as 'no s-process', 'mild s-process enrichment' and 'strong s-process enrichment', see Sect. 5.

of 0.2 dex has been applied to obtain the final adopted O abundance for this object (Asplund et al. 2005; Amarsi et al. 2016). In TYC 2913−1375−1 and TYC 3144−1906−1, we could detect neither the 6300.303 Å line nor the 7774 Å line; hence, we used another α-element, namely Ca, and adopted [Ca/Fe] as a proxy for [O/Fe] (Table A.1).

The carbon abundance is obtained mainly from the CH band at 4310 Å and from the C_2 bands at 5165 and 5635 Å. Since our programme stars do not show strong enrichment of carbon, the C_2 bands are not saturated. We could derive consistent abundances from these three bands.

The nitrogen abundance for the programme stars is derived from the CN molecular lines above 7500 Å. The $^{12}C/^{13}C$ ratio is derived using ^{12}CN features at 8003.553 and 8003.910 Å, and ^{13}CN features at 8004.554, 8004.728, 8004.781, 8010.458, and 8016.429 Å. For several stars, the S/N was not high enough to enable us to estimate the $^{12}C/^{13}C$ ratio.

4.3. Light s-process elements: Sr, Y and Zr

The Y abundances for the programme stars were determined from the Y II lines. The Zr abundance was derived using Zr I

and Zr II lines, which yield consistent abundances. We now present a detailed discussion of all the lines involved in the Sr abundance determination, either in our own work or in N19, as Sr is a key element in N19 barium-star diagnostic. In the present work, the Sr abundance is estimated using the Sr I lines at 4607.327 Å (resonance line), 4811.877 Å (non-resonant) and 7070.070 Å (non-resonant).

For the Sr I line at 4811.877 Å (not used by Karinkuzhi et al. 2018, 2021), a $\log gf$ of 0.190 has been used (García & Campos 1988). For the 4607.327 Sr I line, Hansen et al. (2013) advocate the value of 0.283 for its $\log gf$ (from Parkinson et al. 1976) because it allows to match the solar Sr abundance. An analysis of the HERMES Arcturus spectrum shows a similar agreement as for the Sun, as revealed by the first line of Table 2. Adopting a metallicity of −0.62 for Arcturus (Maeckle et al. 1975), the 4607.327 and 4811.877 lines yield [Sr/Fe] = −0.43 and −0.20, respectively, in agreement with Maeckle et al. (1975) who found [Sr/Fe] = −0.4 ± 0.3 dex.

The Sr I line at 4607.327 Å is known to form under NLTE conditions (Bergemann et al. 2012; Hansen et al. 2013) and Bergemann et al. (2012) list (in their Table 3) the NLTE corrections for this line at metallicities 0.0 and −0.60 for various temperatures and surface gravities. The atmospheric parameters of all our programme stars are within this range and the corresponding NLTE corrections vary between 0.1 and 0.27 dex. In Table 2, we list separately the abundances derived from the three clean (i.e. unblended and not saturated) Sr lines, namely Sr I 4607.327, 4811.877 Å, and 7070.070 Å, along with the NLTE correction (between parentheses) applied to the LTE abundance from the 4607.327 line (for the latter line, Table 2 lists the NLTE abundance). Table A.2 provides the average [Sr/Fe] abundance as derived from these three lines.

To derive the Sr abundances, N19 used the Sr II lines at 4077.077 and 4215.519 Å instead. In stars of solar and mildly subsolar metallicities, as it is the case for all the programme stars, these lines are, however, saturated (Fig. 1; see also Hansen et al. 2013) and could not be used to derive abundances.

Nevertheless, for the sake of comparison, Table 2 lists the Sr abundances provided by N19 for these lines, along with our very uncertain abundance estimate from the 4077.077 Å line. The 4215.519 Å line could not be used to derive even a rough abundance estimate as the spectrum syntheses for the different abundances lie on top of each other (Fig. 1). This situation is attributed to the presence of the strong CN bandhead at λ 4216 Å (Sect. 27 of Gray et al. 2009), which strongly depresses the continuum, especially in stars with enhanced C or N. Figure 2 shows the strong impact of the CN band in the 4215 Å region, even in the absence of the Sr line. We note especially how the 'no Sr + CN' (top panel) and 'Sr + CN' (bottom panel) are barely distinguishable, even at the high resolution of HERMES, which is nearly 50 times the one of LAMOST.

In this respect, it is certainly relevant to note that the three no-s stars, considered as Sr-only by N19 (TYC 3144−1906−1, TYC 4684−2242−1, and HD 7863; see Table 1 and Sect. 5), are precisely those being N-rich (Fig. 3).

4.4. Heavy s-process elements: Ba, La, Ce

We derived Ba abundances in most of the programme stars using the Ba II lines at 5853.673 and 6141.673 Å. For a few objects, as these lines are strong and saturated, the Ba abundance is estimated from the spectral synthesis of the weak Ba II line at 4524.924 Å. Ba lines are strongly affected by hyperfine (HF) splitting. HF splitting data is not available for the 4524.924 Å line, but it was taken into account for the Ba II 5853.673 Å line.

The Ba II lines at 4554.026 and 4934.076 Å are saturated (Fig. 4) and were therefore not considered to derive Ba abundances. Nevertheless, they were used by N19, and are listed in Table 2. When comparing the derived Ba abundances, we conclude that the agreement between the N19 study and ours is much better for Ba than for Sr.

The La abundance is determined mainly using the lines for which HF splitting is available.

As we mentioned earlier, all the lines used are listed in Karinkuzhi et al. (2018, 2021) along with the hfs splitting and isotopic shifts as listed in these references.

4.5. Abundance uncertainties

Abundance uncertainties are calculated for all elements using the methodology described in Karinkuzhi et al. (2018, 2021). Following Eq. (2) from Johnson (2002), the uncertainties on the elemental abundances $\log \epsilon$ are expressed as:

$$\begin{aligned}\sigma^2_{\rm tot} = \sigma^2_{\rm ran} &+ \left(\frac{\partial \log\epsilon}{\partial T}\right)^2 \sigma^2_T + \left(\frac{\partial \log\epsilon}{\partial \log g}\right)^2 \sigma^2_{\log g} \\ &+ \left(\frac{\partial \log\epsilon}{\partial \xi}\right)^2 \sigma^2_\xi + \left(\frac{\partial \log\epsilon}{\partial [{\rm Fe/H}]}\right)^2 \sigma^2_{\rm [Fe/H]} \\ + 2\Bigg[\left(\frac{\partial \log\epsilon}{\partial T}\right)&\left(\frac{\partial \log\epsilon}{\partial \log g}\right)\sigma_{T,\log g} + \left(\frac{\partial \log\epsilon}{\partial \xi}\right)\left(\frac{\partial \log\epsilon}{\partial \log g}\right)\sigma_{\log g,\xi} \\ &+ \left(\frac{\partial \log\epsilon}{\partial \xi}\right)\left(\frac{\partial \log\epsilon}{\partial T}\right)\sigma_{\xi,T}\Bigg],\end{aligned} \tag{1}$$

where σ_T, $\sigma_{\log g}$, and σ_ξ are the typical uncertainties on the atmospheric parameters and are derived by taking the average of the errors listed in Table 1, corresponding to each atmospheric parameter. These values are estimated as σ_T = 33 K, $\sigma_{\log g}$ = 0.26 dex, σ_ξ = 0.06 km s^{-1}. The uncertainty on metallicity was estimated as $\sigma_{\rm [Fe/H]}$ = 0.08 dex. The partial derivatives appearing in Eq. (1) were evaluated in the specific case of BD −07° 402, varying the atmospheric parameters $T_{\rm eff}$, $\log g$, microturbulence ξ, and [Fe/H] by 100 K, 0.5, 0.5 km s^{-1} and 0.5 dex, respectively. The resulting changes in the abundances are presented in Table 3. The covariances $\sigma_{T,\log g}$, $\sigma_{\log g,\xi}$, and $\sigma_{\xi,T}$ are derived by the same method as given by Johnson (2002). In order to calculate $\sigma_{T,\log g}$, we varied the temperature while fixing metallicity and microturbulence, and determined the $\log g$ value required for ensuring the ionization balance. Then using Eq. (3) of Johnson (2002), we derived the covariance $\sigma_{T,\log g}$, finding a value of 1.62. In a similar way, we found $\sigma_{\log g,\xi}$ = −0.02 and $\sigma_{\xi,T}$ = 0.75.

The random error $\sigma_{\rm ran}$ is the line-to-line scatter. For most of the elements, we could use more than four lines to derive the abundances. In that case, we adopted $\sigma_{\rm ran} = \sigma_l/N^{1/2}$, where σ_l is the standard deviation of the abundances derived from all the N lines of the considered element. For the elements for which fewer number of lines are used to derive the abundances, we selected a $\sigma_{\rm ran}$ value as described in Karinkuzhi et al. (2021). The final error on [X/Fe] is derived from:

$$\sigma^2_{\rm [X/Fe]} = \sigma^2_{\rm X} + \sigma^2_{\rm Fe} - 2\,\sigma_{\rm X,Fe}, \tag{2}$$

where $\sigma_{\rm X,Fe}$ is calculated using Eq. (6) from Johnson (2002) with an additional term including $\left(\frac{\partial \log\epsilon}{\partial [{\rm Fe/H}]}\right)$.

Table 2. Line by line abundances of Sr and Ba in the programme stars.

	[Sr I/H]			[Sr II/H]		[Ba II/H]				
λ(Å)	4607.33	4811.88	7070.07	4077.08	4215.52	4524.92	4554.03	4934.08	5853.67	6141.67
Arcturus	−1.05 (0.27)	−0.82								
					No s-process enrichment					
HD 7863	−0.27 (0.2)	−0.27	−0.27	−0.17:	–	0.12	−0.18:	–	−0.18	−0.18
	–	–	–	0.9	0.9	–	0.0	0.1	–	–
HIP 69788	−0.22 (0.1)	0.13	–	−0.17:	–	–	0.12:	0.12:	0.12	–
	–	–	–	0.7	0.5	–	0.7	0.4	–	–
TYC 3144−1906−1	–	−0.12	−0.02	−0.17:	–	–	0.12:	0.12:	−0.18	−0.18
	–		–	1.0	1.0	–	0.2	0.0	–	–
TYC 4684−2242−1	−0.57 (0.2)	–	−0.02	0.13:	–	–	0.12:	0.12:	0.02	0.02
	–	–	–	0.9	0.9	–	−0.1	0.0	–	–
					Mild s-process enrichment					
BD −07°402	−0.27 (0.2)	0.12	−0.17	0.13:	–	–	0.12:	0.22:	0.1	0.1
	–	–	–	0.9	1.0	–	0.0	−0.1	–	–
BD +44°575	–	−0.2	−0.17	−0.17:	–	–	0.12:	0.12:	−0.2	–
	–	–	–	0.9	0.8	–	−0.2	−0.1	–	–
TYC 22−155−1	−0.37 (0.2)	−0.2	0.13	−0.17:	–	0.3:	0.12:	0.12:	0.1	0.1
	–	–	–	0.5	0.5	–	−0.2	−0.3	–	–
	–	–	–	0.2	0.4	–	−0.3	−0.5	–	–
TYC 2913−1375−1	[a]–	–	–	–	–	–	−0.18	−0.03:	−0.68	−0.68
	–	–	–	0.2	0.4	–	−0.3	−0.5	–	–
TYC 3305−571−1	0.30 (0.2)	–	0.13:	–	–	–	0.42:	–	0.32	0.32
	–	–	–	0.9	0.9	–	0.2	0.1	–	–
TYC 752−1944−1	0.03 (0.1)	–	0.43	–	–	–	0.62:	0.62:	0.52	0.52
	–	–	–	0.8	0.8	–	0.3	0.0	–	–
TYC 4837−925−1	−0.27(0.2)	–	0.13	−0.17:	–	–	0.12:	0.12:	−0.18	−0.18
	–	–	–	0.8	0.8	–	0.0	−0.1	–	–
TYC 3423−696−1	0.53: (0.1)	0.43	–	−0.17:	–	–	0.12:	0.12:	0.0	0.1
	–	–	–	0.8	0.9	–	0.1	0.2	–	–
					Strong s-process enrichment					
TYC 2250−1047−1	0.33 (0.2)	0.73	–	–	–	0.62	0.82:	0.82:	0.62	0.62
	–	–	–	−0.8	−0.7	–	0.3	0.3	–	–
TYC 2955−408−1	0.03 (0.2)	–	0.43	0.13:	–	0.6	0.52:	0.52:	0.52	0.52
	–	–	–	0.7	0.6	–	0.2	-0.2	–	–
TYC 591−1090−1	−0.07 (0.1)	–	–	–	–	0.9	0.82:	0.82:	0.6	–
	–	–	–	0.5	−0.4	–	0.7	0.7	–	–

Notes. The first line for each star provides [X/H] abundances from the present paper, and the second line those from N19, which were converted from the original [X/Fe] data using N19 metallicity (as listed in Table 1). [Sr I/H] is the Sr abundance derived from Sr I lines, and similarly for Sr II and Ba II. For the Sun, we adopted $\log \epsilon_{\odot}$(Sr) = 2.87 ± 0.07 and $\log \epsilon_{\odot}$(Ba) = 2.18 ± 0.09, according to Asplund et al. (2009). The value between parentheses in column [Sr I/H] λ 4607.327 is the NLTE correction according to Bergemann et al. (2012), and the Sr abundance listed in that column is NLTE-corrected. For the criteria used to classify stars as 'no s-process', 'mild s-process enrichment' and 'strong s-process enrichment', see Sect. 5. [a]See discussion in Sect. 6.

5. Classification based on abundance ratios

Based on the abundances listed in Table A.2, we classify our programme stars according to the following criteria: 'no' designates objects for which all heavy elements listed in Table A.2 have [X/Fe] < 0.2; 'mild' designates objects for which at least three heavy elements are in the range 0.2 < [X/Fe] < 0.8; 'strong' designates objects for which at least three heavy elements have [X/Fe] ≥ 0.8.

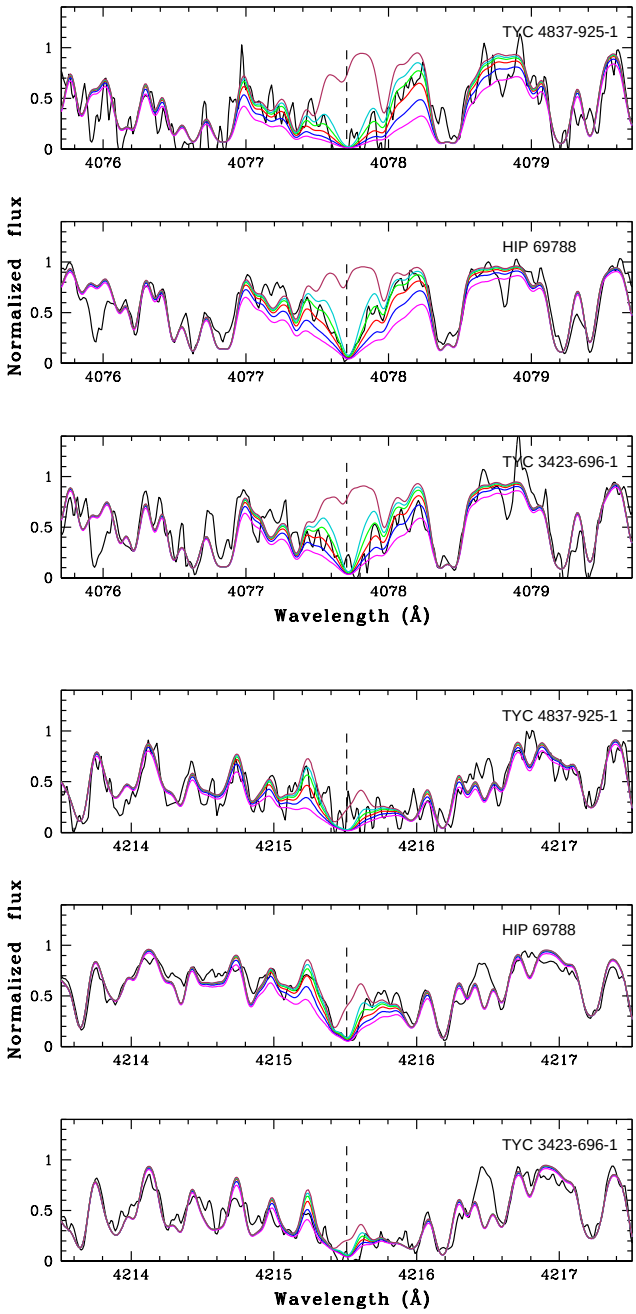

Fig. 1. Sr II 4077.077 Å (*top panel*) and Sr II 4215.519 Å (*bottom panel*) lines are shown in three N19 "Sr-only" stars. The magenta, blue, red, green, and turquoise lines correspond to $\log \epsilon$(Sr) = 3.6, 3.3, 3.0, 2.7, and 2.4 dex, respectively. The brown line is for no Sr. These lines are clearly saturated.

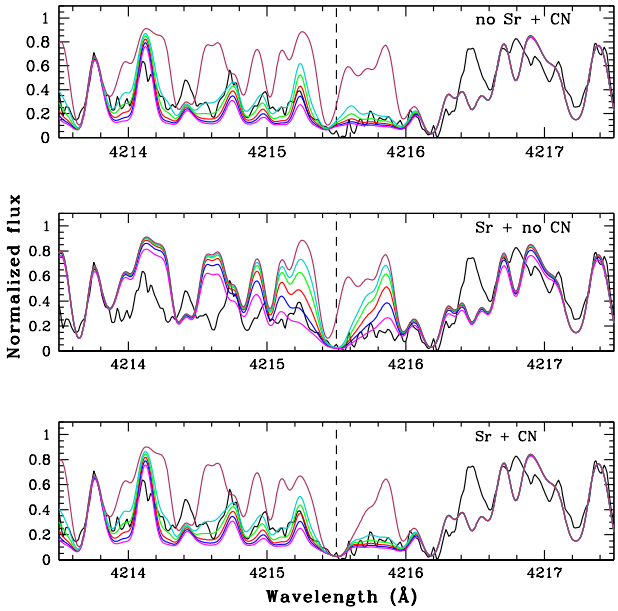

Fig. 2. Spectral syntheses of the 4214–4217 Å wavelength range surrounding the Sr II 4215.519 Å line in HD 7863. *Top panel*: spectral syntheses do not include the Sr II 4215.519 Å line, to reveal the impact of the 4216 Å CN band head. The magenta, blue, red, green and turquoise lines correspond to $\log \epsilon$ (N) = 9.15, 8.85, 8.55, 8.25 and 7.95 dex, respectively. The brown line is a synthesis without N (and no Sr). *Middle panel*: contribution from the CN band is removed and spectral syntheses are computed by varying only the Sr abundance. In this case, the magenta, blue, red, green and turquoise lines correspond to $\log \epsilon$ (Sr) = 3.6, 3.3, 3.0, 2.7 and 2.4 dex, respectively. The brown line is the synthesis without Sr and N. *Bottom panel*: synthesis include both the Sr II 4215.519 Å line and the CN bandhead, with the Sr abundance of Table A.2 ($\log \epsilon$(Sr) = 2.58) and various N abundances, with the same colour-coding as in the top panel. The brown line is the synthesis without N. The adopted ^{12}C/^{13}C ratio is 19.

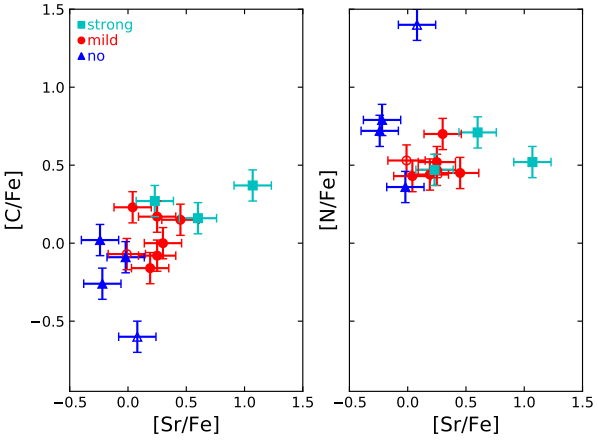

Fig. 3. Correlation between the [Sr/Fe] index and the C and N abundances, showing a clear N overabundance for three among the four Sr-no stars (see Sect. 5).

As shown in Fig. 5, Sr and Ba abundances are correlated (left panel), with just one star (TYC 3423−6966−1) falling the farthest away from the regression line, with a marginal Sr excess ([Sr/Fe] ∼ 0.5) and no Ba excess ([Ba/Fe] ∼ 0). Our analysis thus finds no 'Sr-only' stars (which would correspond to stars with only Sr overabundant – or more generally with only the first-s-process-peak elements overabundant, which are not present in Table A.2), as opposed to the 13 stars flagged as such by N19 (see the right panel of Fig. 5 and Table 1). The 13 'Sr-only' stars of N19 split in 4 'no-s' stars, 8 mild barium stars, and 1 strong barium star.

Figure 6 also reveals that 'no-s' stars cannot be attributed to an unrecognised positive luminosity effect on the Sr II lines (i.e. a low $\log g$, causing a strengthening of lines from ionised species) since these 'no-s' stars are not restricted to low $\log g$ values.

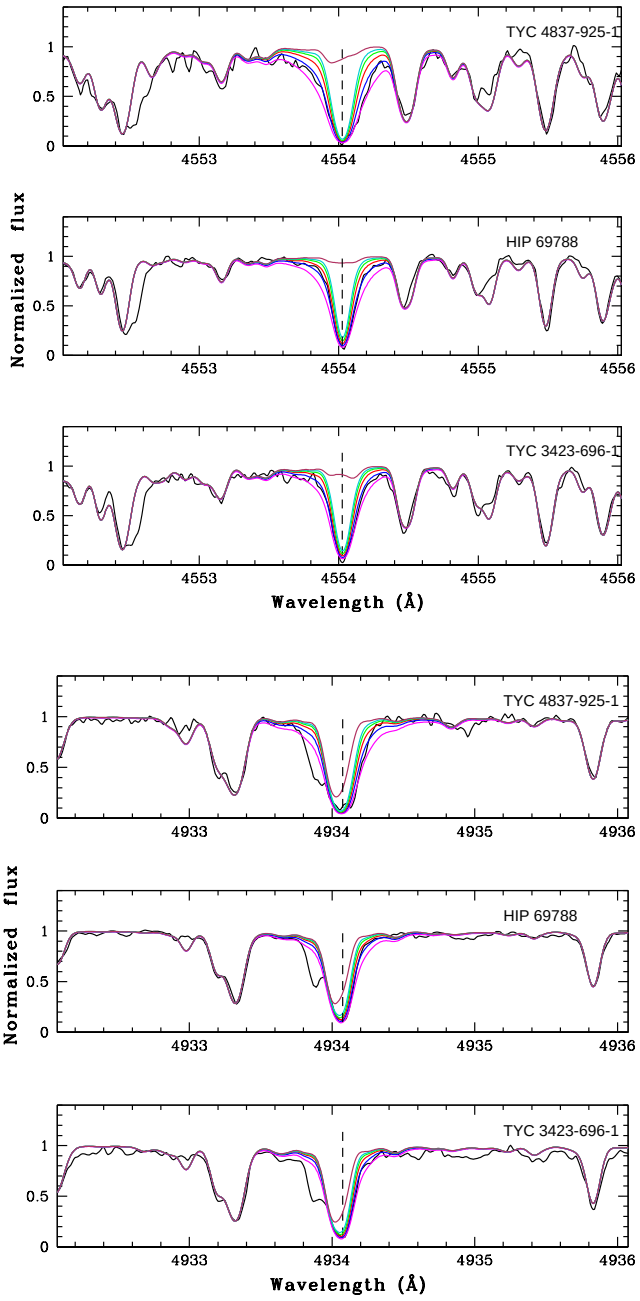

Fig. 4. Ba II 4554.026 Å (*top panel*) and Ba II 4934.076 Å lines (*bottom panel*) are shown in three N19 Sr-only stars. The magenta, blue, red, green, and cyan curves correspond to log ϵ(Ba) = 2.6, 2.3, 2.0, 1.7 and 1.4 dex, respectively. The brown curve is for no Ba.

It is worth noting that the two most enriched barium stars are actually barium dwarfs (Figs. 6 and 7). Curiously enough, in N19 it is mentioned that because their machine-learning algorithm used a training sample composed of giant stars only, they were therefore not able to identify s-process enhanced dwarf stars. Here, we show the contrary, because the 4554.026 Å and 4934.076 Å Ba II lines, though saturated, are apparently sensitive to a Ba enhancement both in giants and dwarfs (in Fig. 4, HIP 69788 and TYC 3423−696−1 are dwarfs whereas TYC 4837−925−1 is a giant). Therefore, the residuals between the observed flux at those wavelengths and *The Cannon* data-driven model will be able to identify barium stars, irrespective of them being dwarfs or giants.

Table 3. Sensitivity of the abundances ($\Delta \log \epsilon_X$) with variations of the atmospheric parameters (considering the atmospheric parameters of BD −07° 402).

	$\Delta \log \epsilon_X$			
Element	$\Delta T_{\rm eff}$ (+100 K)	$\Delta \log g$ (+0.5)	Δ [Fe/H] (+0.5 dex)	$\Delta\xi_t$ (+0.5 km s^{-1})
Li	0.15	0.00	0.00	0.00
C	0.00	0.15	0.10	0.00
N	0.10	0.30	0.30	0.10
O	0.00	0.20	0.15	0.00
Na	0.11	0.08	−0.15	−0.05
Fe	0.13	0.25	0.20	−0.15
Rb	0.00	0.05	−0.05	0.00
Sr	0.30	0.15	0.15	0.00
Y	0.05	0.13	0.03	0.25
Zr	0.03	0.07	−0.08	−0.05
Ba	0.05	0.17	−0.15	−0.40
La	0.00	0.16	0.05	0.04
Ce	0.04	0.20	0.08	−0.05

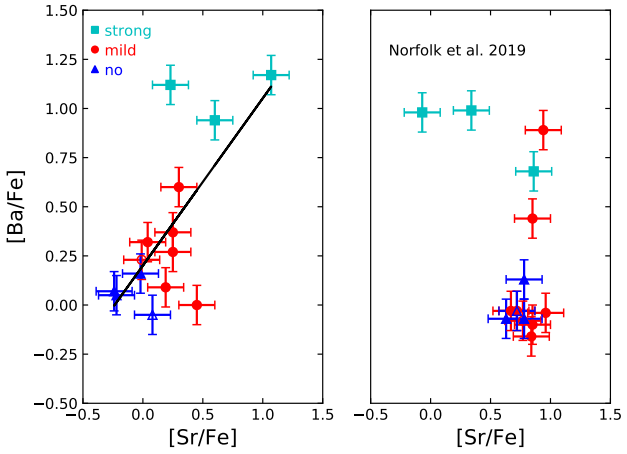

Fig. 5. ([Ba/Fe], [Sr/Fe]) plane from this analysis (*left panel*) and from N19 (*right panel*). The *left panel* reveals that there exists a correlation between the [Sr/Fe] and [Ba/Fe] abundance ratios, represented by the solid line corresponding to a least-square fit to the data. The 'strong', 'mild' and 'no' stars (see Sect. 5) are colour-coded as indicated in the label. Open symbols refer to stars with a Li abundance determination. The *right panel* shows [Ba/Fe] and [Sr/Fe] from N19.

6. Discussion of individual stars

In this section we present additional information for some of the stars re-analyzed in the present paper.

- BD −07°402: this object is the only mild Ba star with a measurable Li abundance of log $\epsilon_{\rm Li}$ = 1.3 dex, just large enough to qualify it as a Li-rich K giant (Jorissen et al. 2020).
- BD +44°575: this mild Ba star presents strong enrichments in Na and Mg.
- HD 7863: this 'no-s' star is one of four objects in our sample that exhibits a larger than average N abundance ([N/Fe] ≥ 0.7; Fig. 3 and Sect. 4.2).
- HIP 69788: this star has atmospheric parameters which differ the most between our study and that of N19 (see Table 1 and Sect. 8).

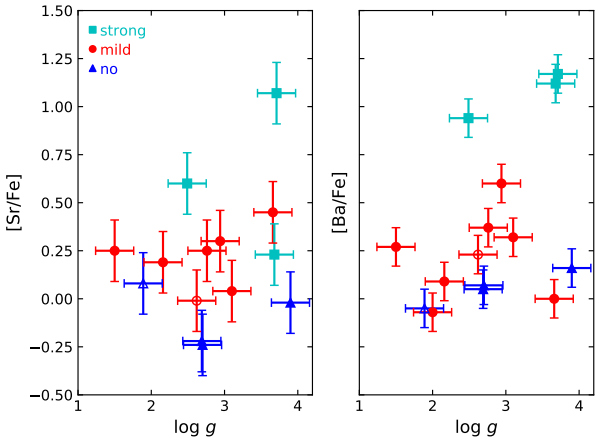

Fig. 6. [Sr/Fe] and [Ba/Fe] abundance ratios versus log g. Symbols are the same as in Fig. 5.

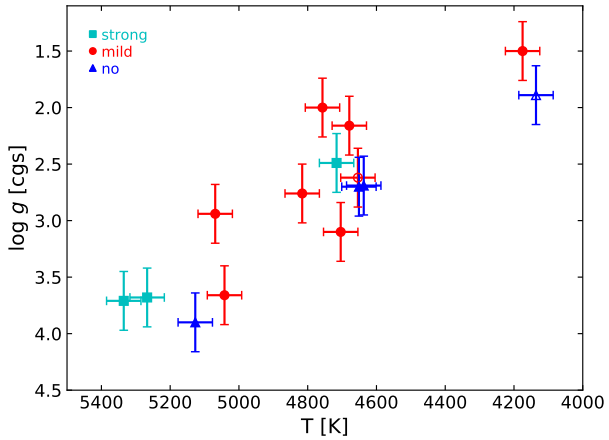

Fig. 7. Kiel diagram (log g vs. $T_{\rm eff}$) for the programme stars.

- TYC 22−155−1: this star exhibits a strong enrichment in Mg.
- TYC 2913−1375−1: for this star, an accurate Sr abundance could not be derived since the Sr I lines are weak and the spectrum is too noisy in the violet to access the Sr II lines. Nevertheless, Zr, Ba, and La lines reveal that this star has mild s-process enhancements.
- TYC 3144−1906−1: this is the second object with a measured Li abundance, but not large enough, however (log $\epsilon_{\rm Li}$ = 0.6 dex), to be considered as a Li-rich K giant. While it is not enriched in any s-process elements, this star shows a high enhancement in N ([N/Fe] = 1.40 dex; Fig. 3).
- TYC 4684−2242−1: another 'no-s' star with a larger than average N abundance (Fig. 3). It is worth noting that three out the four N-rich stars ([N/Fe] ≥ 0.7) do not show any s-process enhancement.

7. Origin of the peculiarities of mild and strong barium stars

7.1. Binary frequency

According to the canonical scenario (McClure 1983; Jorissen et al. 2019; Escorza et al. 2019), barium stars form in a binary system. Table 4 therefore collects the kinematical properties of our programme stars. Contrary to what is asserted in their paper, N19 do not provide the LAMOST radial velocities (RVs) in their supplementary material. Therefore, we resorted to *Gaia* Data Release 2 (GDR2; Katz et al. 2019) to obtain a RV value to compare with the HERMES value. GDR2 velocities refer to epoch 2015.5 (JD 2 457 205), whereas HERMES RVs were taken roughly 1700 d later, offering a large enough time span to efficiently detect even long-period binaries.

The uncertainty ϵ (listed in Table 4) on the GDR2 RVs was computed from $G_{\rm RVS}$ (the *Gaia* magnitude in the RVS band) along the same method as discussed by Jorissen et al. (2020, their Eqs. (3) and (4)), except that Eq. (4) has been replaced by one depending on the *Tycho* $B_T - V_T$ colour index, as listed in Table 7 of Jordi (2018). As can be seen in Table 4, uncertainties on the GDR2 RVs are on the order of 0.3 km s^{-1} for the brightest targets ($G_{\rm RVS} \sim 8$) and go up to 1 km s^{-1} for the faintest objects ($G_{\rm RVS} \sim 10.8$). We note that most of the stars have the computed ϵ uncertainty very similar to the RV uncertainty listed by GDR2 (except for the binary HIP 69788). Based on the above, we have flagged as binaries all stars with $\Delta{\rm RV} \geq 3\,\epsilon$.

As expected, 2 out of 3 strong barium stars show a clear binary signature and the third one (TYC 591−1090−1) is the faintest in the sample, and despite its large ΔRV value of 1.55 km s^{-1}, it does not fulfill the 3ϵ condition. The results for the other classes are intriguing, since only 1 of the 7 mild barium stars diagnosed exhibit statistically significant RV variations, and on the opposite, 2 out of the 4 'no-s' stars show a binary signature.

We see no obvious explanation for the high prevalence of binaries among the latter category, other than small-number fluctuations. Concerning the mild Ba stars, it is still possible that their RV variations are more difficult to detect since they contain a larger proportion of binaries with very long periods (>5000 d) than strong barium stars do (see Fig. 7 of Jorissen et al. 2019), thus explaining the lower apparent frequency of binary signatures among mild barium stars. Alternatively, some mild barium stars with no binary signature might represent the upper tail of the [Ba/Fe] range in the Galactic ([Ba/Fe], [Fe/H]) trend (Edvardsson et al. 1993). Such mild barium stars are especially present at metallicities in the range [−0.4, +0.1] dex (Fig. 15 panel k of Edvardsson et al. 1993, Fig. 5 of Tautvaišienė et al. 2021).

All non-binary mild barium stars but TYC 2913−1375−1 have [Fe/H] in the above range, making it likely that they owe their mild-barium nature to the fluctuations in the Galactic chemical evolution. Figure 8, which displays the Toomre diagram of the programme stars, reveals no difference in their kinematic properties and shows that they all belong to the Galactic thin disc.

7.2. Location in the HRD

Figure 9 presents the location of our programme stars in the Hertzsprung-Russell diagram (HRD). In this plot, we used the spectroscopic $T_{\rm eff}$ values listed in Table 1 and determined the luminosity of each target by combining the flux obtained from integrating their spectral energy distributions (SED) with the distances computed by Bailer-Jones et al. (2021) from the *Gaia* Early Data Release 3 parallaxes (Gaia Collaboration 2021). To build and fit the SEDs, we applied the methodology described by Escorza et al. (2017) and successfully used in combination with spectroscopic parameters. The tool performs a χ^2-grid-search to find the best-fitting MARCS model atmosphere (Gustafsson et al. 2008) to the available broadband photometry for each

Table 4. Kinematic properties of the programme stars.

Name	JD (−2 400 000)	RV (km s^{-1})	ΔRV (km s^{-1})	ϵ (km s^{-1})	$G_{\rm RVS}$	source	U (km s^{-1})	V (km s^{-1})	W (km s^{-1})	*Gaia* DR2	Bin./Rem.
No s-process enrichment											
HD 7863	57 205	−27.82 ± 0.34	0.45	0.29	8.09	GDR2	24.95	−23.58	−13.81	397523176280439808	n
	58 882.41	−28.27 ± 0.07				HER					
HIP 69788	57 205	6.56 ± 1.94	55.93	0.42	9.39	GDR2	31.08	11.94	−9.27	3667671452515762944	y[(a)]
	58 877.70	−49.37 ± 0.07				HER					
TYC 3144−1906−1	57 205	−21.56 ± 0.33	1.06	0.28	7.84	GDR2	−20.73	−16.47	−5.61	2077143186195922176	y
	59 090.45	−22.62 ± 0.07				HER					
TYC 4684−2242−1	57 205	36.53 ± 0.44	0.92	0.41	9.35	GDR2	−66.36	6.01	−15.01	2478965826587133568	n
	58 882.33	35.61 ± 0.07				HER					
Mild s-process enrichment											
BD −07° 402	57 205	−12.96 ± 0.17	0.48	0.29	8.04	GDR2	4.72	−2.66	12.05	2486894817251498240	n
	58 882.37	−13.44 ± 0.07				HER					
BD +44° 575	57 205	−12.61 ± 0.26	0.50	0.28	7.78	GDR2	28.21	17.09	1.94	340768207120632832	n
	58 878.41	−13.11 ± 0.07				HER					
TYC 22−155−1	57 205	−37.70 ± 0.58	0.35	0.33	8.71	GDR2	−48.38	−65.05	32.26	2539172197106047872	n
	58 882.36	−38.05 ± 0.07				HER					
TYC 2913−1375−1	57205	−2.89 ± 0.42	0.15	0.48	9.70	GDR2	2.22	−14.52	44.81	1937033729462492 16	n
	59 090.71	−3.04 ± 0.07				HER					
TYC 3305−571−1	57 205	−57.93 ± 0.33	0.52	0.37	9.08	GDR2	30.31	−55.92	3.80	437946515118550016	n
	58 878.48	−58.45 ± 0.07				HER					
TYC 4837−925−1	57 205	−22.91 ± 0.23	0.52	0.37	9.11	GDR2	35.55	−8.52	−13.98	3081162263449705984	n
	58 877.55	−23.43 ± 0.07				HER					
TYC 3423−696−1	57 205	5.37 ± 0.21	−3.16	0.40	9.26	GDR2	−21.20	−55.96	−2.78	1016739606459940608	y
	58 877.61	8.53 ± 0.07				HER					
TYC 752−1944−1	58 877.49	19.04 ± 0.07	–			HER	4.66	−17.38	−29.26	3157928756551254400	?
Strong s-process enrichment											
TYC 2250−1047−1	57 205	19.39 ± 0.75	3.44	0.75	10.41	GDR2	−76.78	4.84	−9.30	2839977000550809856	y
	59 090.61	15.95 ± 0.07				HER					
TYC 2955−408−1	57 205	41.15 ± 0.56	2.07	0.42	9.41	GDR2	−61.94	−6.77	−42.54	953203601197511808	y
	58 879.54	39.08 ± 0.07				HER					
TYC 591−1090−1	57205	8.80 ± 0.88	1.55	1.00	10.83	GDR2	41.23	26.56	9.10	2757528128276067840	n
	59 090.64	7.25 ± 0.07				HER					

Notes. In column 'source', GDR2 stands for *Gaia* Data Release 2, and 'HER' for HERMES. ΔRV is the difference between the HERMES and GDR2 radial velocities. ϵ is the uncertainty on the GDR2 RV, computed as explained in the text. $G_{\rm RVS}$ is the magnitude in the RVS band (Jordi 2018). U, V, W are the Cartesian components of the velocity in Galactic coordinates, taken from N19. The *Gaia* DR2 identifier has been listed to ease the cross match with N19 data table. For the criteria used to classify stars as 'no s-process', 'mild s-process enrichment' and 'strong s-process enrichment', see Sect. 5. [(a)]Also proper motion anomaly (Kervella et al. 2019).

target collected from the SIMBAD database (Wenger et al. 2000), treating the total line-of-sight reddening E_{B-V} as a free parameter for which we optimise. We used the parameter ranges obtained from the spectroscopic analysis to limit $T_{\rm eff}$ and $\log g$, and we fixed the metallicity to the closest available in the MARCS grid (0.0, −0.25 or −0.5 for our targets), leaving E_{B-V} as the only fully unconstrained parameter. Then each best-fitting SED model is corrected for interstellar extinction assuming that the line-of-sight extinction A_V follows the Galactic extinction law given by $A_V = R_V \times E_{B-V}$ with $R_V = 3.1$ (Fitzpatrick 1999). The SED is then integrated to get the total flux.

The star locations in the HRD are compared with evolutionary tracks from STAREVOL (Siess & Arnould 2008) for three metallicities, [Fe/H] = −0.5, −0.25, and 0. A correlation may seem to exist between mass and metallicity: at the lowest metallicity [Fe/H]= −0.5 (panel a of Fig. 9), barium stars are found in the full mass range 1.2–3 $M_\odot$, whereas at solar metallicity (panel c of Fig. 9), they are restricted to the much narrower range 0.9–1.5 $M_\odot$. This correlation is not confirmed, however, by the larger sample studied by Jorissen et al. (2019, their Fig. 17). Thus, the segregation observed in Fig. 9 is likely the result of small-sample statistics. To summarize, the confirmed barium stars from N19 are found in the mass range 0.9–3 $M_\odot$ and are located all the way from the end of the main-sequence till the red clump through the red-giant phase.

7.3. Abundance trends

In most of the barium stars studied here, the second s-process peak reaches slightly larger overabundance levels than the first

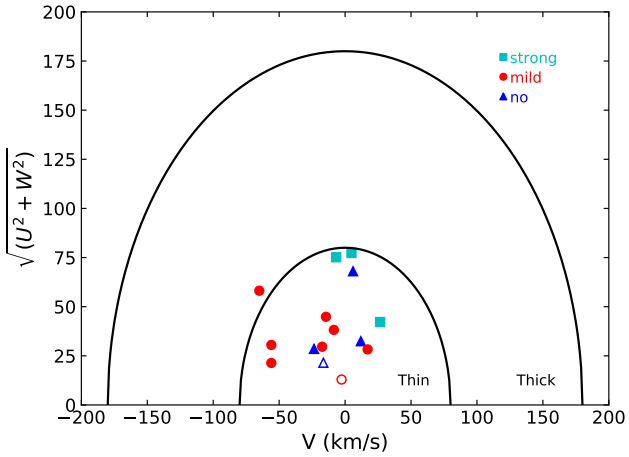

Fig. 8. Toomre diagram of the programme stars, with the black line delineating the location of thin-disk stars (as in Fig. 4 of N19).

peak, resulting in [hs/ls] ratios ranging from 0 to 0.5 dex (Fig. 10), with only two exceptions (TYC 3423−696−1 and TYC 2955−408−1), where [hs/ls] = −0.1. As usual in barium stars, the [hs/ls] ratio does not show a strong correlation with metallicity (right panel of Fig. 10).

The distribution of [La/Fe] vs [Fe/H] (right panel of Fig. 11) indicates that there might be a weak correlation between metallicity and the level of s-process enrichment since strong barium stars with [La/Fe] ≥ 0.75 have [Fe/H] ≤ −0.30, whereas mild barium stars cluster instead around a slightly subsolar metallicity ([Fe/H] ∼ −0.1). As explained in Sect. 4.3, 'no-s' stars show comparatively large enhancements in N and hence low [C/N] values (Fig. 12). The low [C/N] values in these stars may be the result of an efficient mixing as they ascend the first giant branch (RGB) since their [N/Fe] ratio increases with luminosity along the RGB.

8. Automatic vs. manual classification

Table 1 reveals that 4 stars out of 15 have in fact been erroneously flagged as mild barium stars by the machine-learning method used by N19. The topic of this section is to identify what might be learned about the power of such machine-learning methods: we consider whether we can identify why machine-learning led to such a large fraction of 'false positives'. In addition we examine the properties of these false positives with respect to either the accuracy of the atmospheric parameters delivered by *The Cannon* or the properties of the Ba and Sr lines used (are they saturated or not?).

Table 1 compares the atmospheric parameters obtained by N19 and by our high-resolution abundance study. Effective temperatures and gravities are generally in good agreement (the worst discrepancy is 200 K for $T_{\rm eff}$ in HIP 69788 and TYC 2250–1047–1, and 1 dex for the gravity of HIP 69788). The metallicities are more discrepant, up to 0.3 dex (HIP 69788, BD +44°575, and TYC 4837−925−1). However, these discrepant atmospheric parameters are not restricted to those cases where we found no s-process enrichments. Therefore, we believe that false positives do not result from possible inaccuracies in the machine-learning atmospheric parameters.

N19 used strong Sr II and Ba II lines to derive Sr and Ba abundances. From the Sr II lines at 4077 and 4215 Å, N19 found

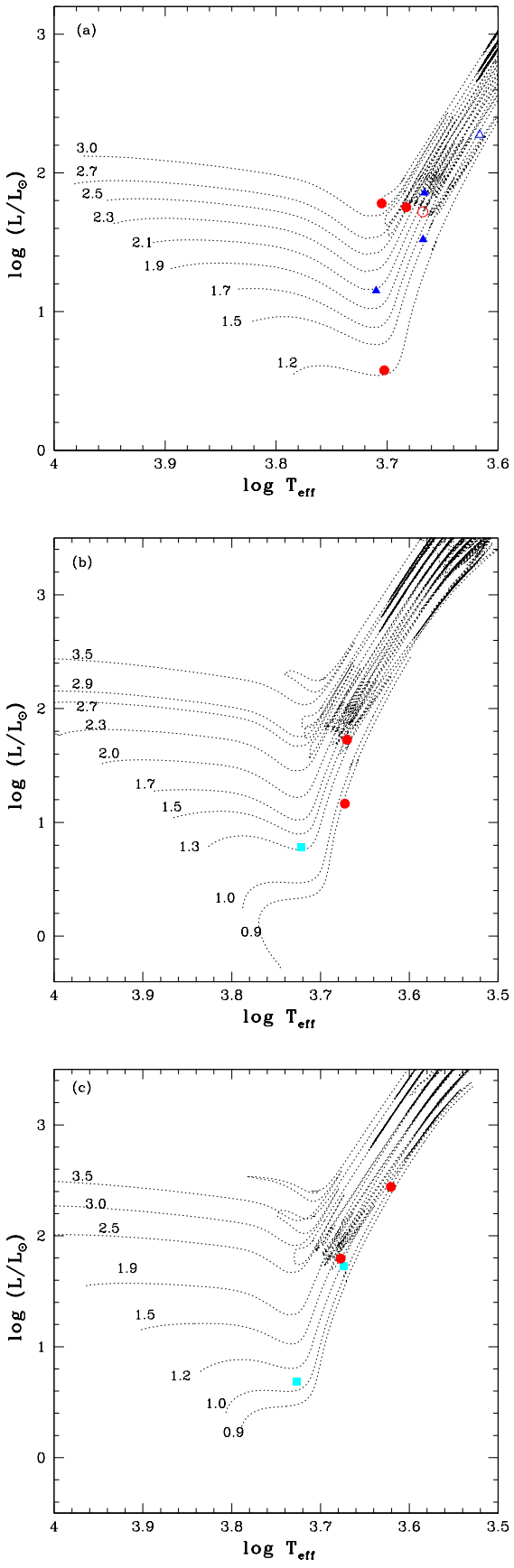

Fig. 9. Location of barium stars in the HRD compared with STAREVOL tracks: (*a*) [Fe/H] = 0 (*b*) [Fe/H] = − 0.25 (*c*) [Fe/H] = −0.5. Symbols are as in Fig. 3.

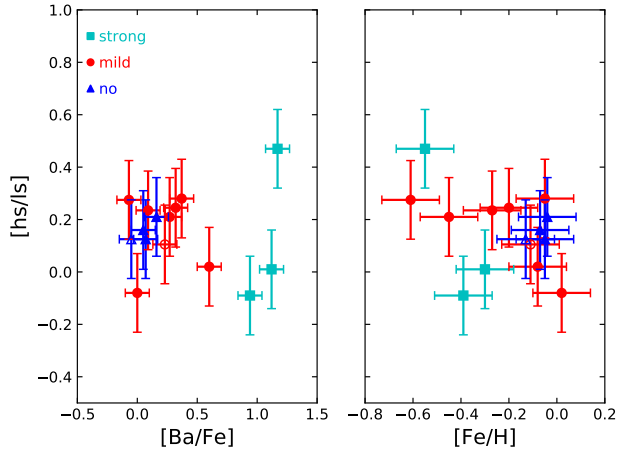

Fig. 10. [hs/ls] ratio as a function of various abundance ratios.

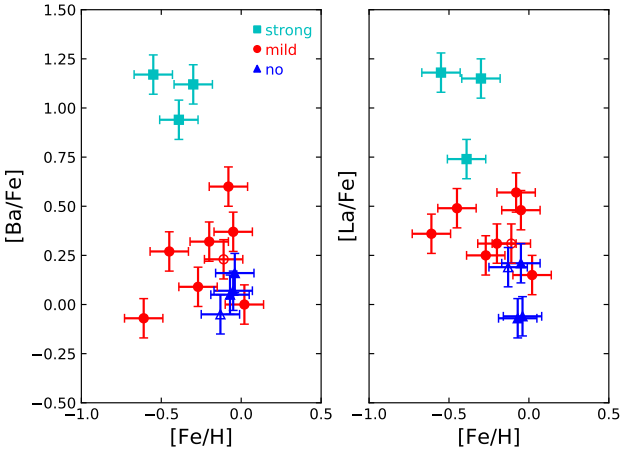

Fig. 11. [Ba/Fe] and [La/Fe] ratios as a function of metallicity [Fe/H].

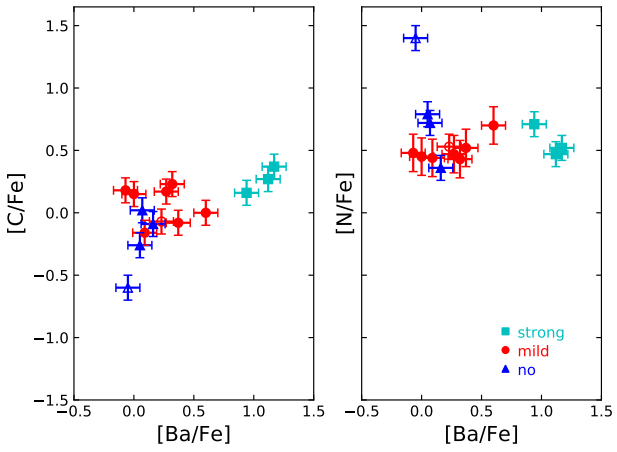

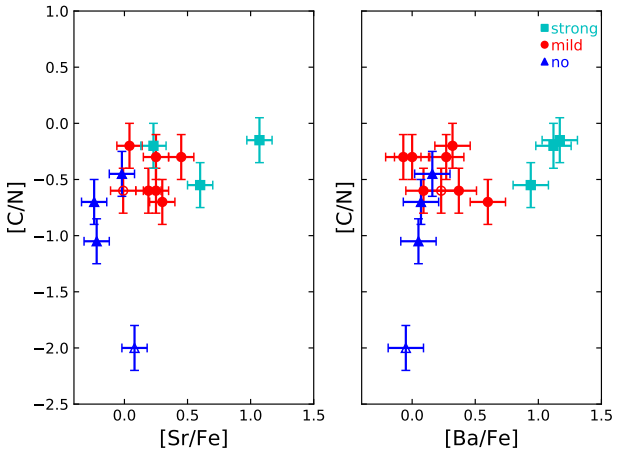

Fig. 12. Various diagnostics involving C and N.

[Sr/Fe] values in the range 0.8–1.0 dex for the four stars with no s-process enrichment in our analysis. Figure 1 reveals that the Sr II line at 4215 Å used by N19 is not only saturated, but also blended by the CN band with its band head at 4216 Å. When this band is strong (i.e. in K giants with a large N abundance [N/Fe] $\geq$ 0.7), it likely causes false 'Sr-only' positives.

9. Conclusions

In this study, we carry out a detailed abundance analysis of fifteen suspected Ba stars from N19. It was found that 3 of them are strongly enhanced with s-process elements, while 8 are mildly enhanced and the remaining 4 show no enhancement in s-process elements. The machine-learning technique used earlier by N19 on low-resolution LAMOST spectra classified thirteen among these fifteen stars as Sr-only candidates. Instead, our traditional approach based on an individual spectroscopic analysis of high-resolution spectra revealed that four of these thirteen stars do not have significant overabundances of any s-process elements. We investigated the possible reasons for the high incidence of the Sr-abundance tag obtained by the machine-learning technique. We found that the Sr lines used by N19 are generally saturated, thus leading to spurious overabundances. Neither has the possibility of a nitrogen enhancement in these stars, as revealed by our analysis, been considered by the N19 analysis. Because of the blend between the Sr II 4215.5 Å line and the CN band head, a high N abundance, if overlooked, may lead to spurious Sr overabundances.

We spectroscopically identified 2 strong Ba dwarfs in the sample, further confirmed by their location in the HR diagram. We found significant radial velocity variations in 5 objects: 2 in the strong Ba class, 1 in the mild Ba class, and more surprisingly, 2 in the no-s class. All the sample stars have Galactic thin-disk kinematic signatures, as made evident from their location in the Toomre diagram. We also compared the properties of mild and strong Ba stars. Various heavy-s abundances revealed a sensitivity to metallicity since all strong Ba stars have sub-solar metallicities. Carbon and N abundances seem to behave differently in the 2 groups, with non-Ba stars having a tendency to be C-poor but N-rich.

Acknowledgements. D.K. acknowledges the financial support from CSIR-India through file No.13(9086-A)2019-Pool. S.V.E. thanks the Fondation ULB for its support. The *Mercator* telescope is operated thanks to grant number G.0C31.13 of the FWO under the "Big Science" initiative of the Flemish governement. Based on observations obtained with the HERMES spectrograph, supported by the Fund for Scientific Research of Flanders (FWO), the Research Council of K.U.Leuven, the Fonds National de la Recherche Scientifique (F.R.S.– FNRS), Belgium, the Royal Observatory of Belgium, the Observatoire de Genève, Switzerland and the Thüringer Landessternwarte Tautenburg, Germany. This research has made use of the SIMBAD database, operated at CDS, Strasbourg,

France and NASA ADS, USA. L.S. and S.G. are senior research associates from F.R.S.- FNRS (Belgium).

References

Alvarez, R., & Plez, B. 1998, A&A, 330, 1109
Amarsi, A. M., Asplund, M., Collet, R., & Leenaarts, J. 2016, MNRAS, 455, 3735
Asplund, M., Grevesse, N., Sauval, A. J., Allende Prieto, C., & Kiselman, D. 2005, A&A, 435, 339
Asplund, M., Grevesse, N., Sauval, A. J., & Scott, P. 2009, ARA&A, 47, 481
Bai, Y., Luo, A. L., Comte, G., et al. 2016, Res. Astron. Astrophys., 16, 107
Bailer-Jones, C. A. L., Rybizki, J., Fouesneau, M., Demleitner, M., & Andrae, R. 2021, AJ, 161, 147
Bergemann, M., Hansen, C. J., Bautista, M., & Ruchti, G. 2012, A&A, 546, A90
Bidelman, W. P., & Keenan, P. C. 1951, ApJ, 114, 473
Edvardsson, B., Andersen, J., Gustafsson, B., et al. 1993, A&A, 500, 391
Escorza, A., Boffin, H. M. J., Jorissen, A., et al. 2017, A&A, 608, A100
Escorza, A., Karinkuzhi, D., Jorissen, A., et al. 2019, A&A, 626, A128
Fitzpatrick, E. L. 1999, PASP, 111, 63
Gaia Collaboration (Brown, A. G. A., et al.) 2021, A&A, 649, A1
García, G., & Campos, J. 1988, J. Quant. Specrtr. Rad. Tnansf., 39, 477
Gray, R. O., Corbally, C. J., & Burgasser, A. J. 2009, Stellar Spectral Classification (Princeton: Princeton University Press)
Gustafsson, B., Edvardsson, B., Eriksson, K., et al. 2008, A&A, 486, 951
Hansen, C. J., Bergemann, M., Cescutti, G., et al. 2013, A&A, 551, A57
Hansen, C. J., Nordström, B., Hansen, T. T., et al. 2016, A&A, 588, A37
Hansen, C. J., Hansen, T. T., Koch, A., et al. 2019, A&A, 623, A128
Heiter, U. 2020, in IAU General Assembly, 458
Heiter, U., Lind, K., Asplund, M., et al. 2015, Phys. Scr, 90, 054010
Johnson, J. A. 2002, ApJS, 139, 219
Jordi, C. 2018, *Gaia* DPAC report GAIA-C5-TN-UB-CJ-041
Jorissen, A., Boffin, H. M. J., Karinkuzhi, D., et al. 2019, A&A, 626, A127
Jorissen, A., Van Winckel, H., Siess, L., et al. 2020, A&A, 639, A7
Karinkuzhi, D., Van Eck, S., Jorissen, A., et al. 2018, A&A, 618, A32
Karinkuzhi, D., Van Eck, S., Goriely, S., et al. 2021, A&A, 645, A61
Katz, D., Sartoretti, P., Cropper, M., et al. 2019, A&A, 622, A205
Kervella, P., Arenou, F., Mignard, F., & Thévenin, F. 2019, A&A, 623, A72
Lü, P. K. 1991, AJ, 101, 2229
Lü, P. K., Dawson, D. W., Upgren, A. R., & Weis, E. W. 1983, ApJS, 52, 169
MacConnell, D. J., Frye, R. L., & Upgren, A. R. 1972, AJ, 77, 384
Maeckle, R., Holweger, H., Griffin, R., & Griffin, R. 1975, A&A, 38, 239
Masseron, T., Merle, T., & Hawkins, K. 2016, Astrophysics Source Code Library [record ascl:1605.004]
McClure, R. D. 1983, ApJ, 268, 264
Ness, M., Hogg, D. W., Rix, H. W., Ho, A. Y. Q., & Zasowski, G. 2015, ApJ, 808, 16
Norfolk, B. J., Casey, A. R., Karakas, A. I., et al. 2019, MNRAS, 490, 2219
Parkinson, W. H., Reeves, E. M., & Tomkins, F. S. 1976, J. Phys. B, 9, 157
Plez, B. 2012, Astrophysics Source Code Library [record ascl:1205.004]
Raskin, G., van Winckel, H., Hensberge, H., et al. 2011, A&A, 526, A69
Siess, L., & Arnould, M. 2008, A&A, 489, 395
Smiljanic, R., Porto de Mello, G. F., & da Silva, L. 2007, A&A, 468, 679
Tautvaišienė, G., Viscasillas Vázquez, C., Mikolaitis, Š., et al. 2021, A&A, 649, A126
Warner, B. 1965, MNRAS, 129, 263
Wenger, M., Ochsenbein, F., Egret, D., et al. 2000, A&AS, 143, 9
Wu, Y., Luo, A. L., Li, H.-N., et al. 2011, Res. Astron. Astrophys., 11, 924

Appendix A: Abundances

The following tables present the elemental abundances of the programme stars. NLTE abundance corrections are applied when available, that is, for Sr. We used the same atomic and molecular lines presented in Karinkuzhi et al. (2018, 2021).

Table A.1. Light element abundances.

Star Name	[Ca/Fe]	[Sc/Fe]	[Ti/Fe]	[V/Fe]	[Cr/Fe]	[Ni/Fe]	[Cu/Fe]	[Zn/Fe]
HD 7863	0.03	–	0.12	0.44	0.03	−0.30	−0.22	−0.49
HIP 69788	0.30	–0.01	0.09	–0.26	0.40	−0.03	0.15	0.03
TYC 3144−1906−1	−0.21	−0.02	–0.12	0.08	0.09	−0.24	−0.06	−0.43
TYC 4684−2242−1	0.26	0.05	0.25	0.47	0.21	−0.07	0.11	−0.11
BD−07 402	0.07	0.11	0.16	0.38	0.11	−0.01	0.07	0.05
BD+44 575	0.41	0.15	0.50	–	0.41	0.01	0.01	−0.31
TYC 22−155−1	0.36	–	0.40	0.47	0.16	0.13	0.21	0.24
TYC 2913−1375−1	0.27	0.06	0.01	0.06	0.57	0.39	0.11	0.08
TYC 3305−571−1	0.31	0.20	0.10	0.05	0.10	−0.17	0.21	0.09
TYC 752−1944−1	0.04	–	−0.17	0.05	0.14	0.01	−0.11	0.02
TYC 4837−925−1	0.03	0.22	0.17	0.19	0.28	0.05	−0.02	−0.04
TYC 3423−696−1	0.24	–	0.23	0.45	–	−0.24	0.09	−0.03
TYC 2250−1047−1	0.21	0.20	0.20	0.30	0.31	0.03	−0.24	0.19
TYC 2955−408−1	0.35	–	0.24	–	0.35	–	0.20	0.43
TYC 591−1090−1	0.21	0.15	0.20	0.10	0.36	−0.22	0.11	−0.26

Table A.2. Elemental abundances

			BD −07°402			BD +44°575			HD 7863		
	Z	$\log_\odot\epsilon^a$	logϵ	σ_l (N)	[X/Fe] ± σ_t	logϵ	σ_l(N)	[X/Fe] ± σ_t	logϵ	σ_l(N)	[X/Fe] ± σ_t
Li	3	1.05	1.30	0.1(1)	0.36 ± 0.18	–	–	–	–	–	–
C	6	8.43	8.25	0.1(4)	−0.07 ± 0.11	8.15	0.10(4)	0.17 ± 0.11	8.10	0.10(1)	−0.26 ± 0.13
$^{12}C/^{13}C$	–	–	–	–	19	–	–	13	–	–	19
N	7	7.83	8.25	0.1(10)	0.53 ± 0.06	7.85	0.05(15)	0.47 ± 0.05	8.55	0.02(12)	0.79 ± 0.05
O	8	8.69	8.8	0.1(1)	0.22 ± 0.12	8.60	0.10(1)	0.36 ± 0.13	8.65	0.10(1)	0.03 ± 0.12
Na	11	6.24	6.53	0.08(2)	0.40 ± 0.12	6.38	0.08(2)	0.59 ± 0.12	6.44	0.11(4)	0.27 ± 0.12
Mg	12	7.60	–	–	–	8.10:	0.10(2)	0.90 ± 0.15	7.44	0.10(3)	−0.09 ± 0.15
Rb	37	2.52	2.50	0.10(2)	0.09 ± 0.16	–	–	–	2.30	0.10(2)	−0.15 ± 0.16
Sr	38	2.87	2.75	0.16(3)	−0.01 ± 0.13	2.67	0.00(2)	0.25 ± 0.11	2.58	0.10(3)	−0.22 ± 0.10
Y	39	2.21	2.09	0.14(7)	−0.01 ± 0.14	1.72	0.04(6)	−0.04 ± 0.13	1.76	0.20(9)	−0.38 ± 0.14
Zr	40	2.58	2.75	0.07(3)	0.28 ± 0.13	2.61	0.04(4)	0.48 ± 0.12	2.50	0.10(2)	−0.15 ± 0.14
Nb	41	1.46	–	–	–	1.48	0.12(3)	0.47 ± 0.15	–	–	-
Ba	56	2.18	2.30	0.1(2)	0.23 ± 0.07	2.00	0.10(1)	0.27 ± 0.10	2.15	0.15(4)	0.05 ± 0.08
La	57	1.10	1.30	0.10(6)	0.31 ± 0.10	1.14	0.05(8)	0.49 ± 0.09	0.96	0.06(4)	−0.07 ± 0.10
Ce	58	1.58	1.64	0.08(6)	0.17 ± 0.07	1.50	0.10(4)	0.37 ± 0.08	1.34	0.12(7)	−0.14 ± 0.07

			HIP 69788			TYC 22−155−1			TYC 2250−1047−1		
	Z	$\log_\odot\epsilon^a$	logϵ	σ_l(N)	[X/Fe] ± σ_t	logϵ	σ_l(N)	[X/Fe] ± σ_t	logϵ	σ_l(N)	[X/Fe] ± σ_t
C	6	8.43	8.30	0.10(4)	−0.09 ± 0.11	8.45	0.10(4)	0.23 ± 0.11	8.25	0.10(4)	0.37 ± 0.11
N	7	7.83	8.15	0.05(15)	0.36 ± 0.05	8.05	0.10(9)	0.43 ± 0.06	7.80	0.10(10)	0.52 ± 0.06
O	8	8.69	8.90	0.10(2)	0.25 ± 0.10	8.90	0.10(1)	0.44 ± 0.13	8.60	0.10(1)	0.46 ± 0.13
Na	11	6.24	6.30	0.10(2)	0.10 ± 0.13	6.35	0.05(2)	0.31 ± 0.11	5.85	0.10(2)	0.16 ± 0.13
Mg	12	7.60	–	–	–	8.60:	0.10(1)	1.20 ± 0.15	–	–	–
Rb	37	2.52	2.50	0.10(2)	0.02 ± 0.16	–	–	–	2.10	0.10(1)	0.13 ± 0.17
Sr	38	2.87	2.81	0.16(2)	−0.02 ± 0.15	2.71	0.19(3)	0.04 ± 0.14	3.39	0.19(2)	1.07 ± 0.16
Y	39	2.21	1.79	0.09(5)	−0.38 ± 0.13	1.78	0.06(4)	−0.23 ± 0.13	2.10	0.13(5)	0.44 ± 0.14
Zr	40	2.58	2.20	0.10(3)	−0.34 ± 0.13	2.55	0.05(4)	0.17 ± 0.12	2.80	0.10(2)	0.77 ± 0.14
Ba	56	2.18	2.30	0.10(1)	0.16 ± 0.10	2.30	0.10(2)	0.32 ± 0.07	2.80	0.10(3)	1.17 ± 0.07
La	57	1.10	1.00	0.10(4)	−0.06 ± 0.11	1.21	0.12(9)	0.31 ± 0.10	1.73	0.11(8)	1.18 ± 0.10
Ce	58	1.58	1.30	0.10(2)	−0.24 ± 0.09	1.50	0.10(2)	0.12 ± 0.09	2.00	0.07(4)	0.97 ± 0.07

[a] Asplund et al. (2009)
: Uncertain abundances due to a noisy or blended region

Table A.2. Elemental abundances.

			TYC 2913−1375−1			TYC 2955−408−1			TYC 3144−1906−1		
	Z	$\log_\odot\epsilon^a$	$\log\epsilon$	σ_l (N)	[X/Fe] ± σ_t	$\log\epsilon$	σ_l(N)	[X/Fe] ± σ_t	$\log\epsilon$	σ_l(N)	[X/Fe] ± σ_t
Li	3	1.05	–	–	–	–	–	–	0.60	0.10(1)	−0.32 ± 0.18
C	6	8.43	8.00	0.10(3)	0.18 ± 0.11	8.20	0.10(4)	0.16 ± 0.11	7.70	0.10(1)	−0.60 ± 0.14
N	7	7.83	7.70	0.10(10)	0.48 ± 0.06	8.15	0.06(15)	0.71 ± 0.05	9.10	0.05(15)	1.40 ± 0.11
O	8	8.69	–	–	–	8.60	0.10(1)	0.33 ± 0.13	–	–	–
Na	11	6.24	8.60	0.10(1)	0.52 ± 0.15	6.15	0.10(2)	0.30 ± 0.13	6.60	0.10(2)	0.49 ± 0.13
Mg	12	7.60	–	–	–	8.20	0.10(3)	0.99 ± 0.15	–	–	–
Rb	37	2.52	–	–	–	2.48	0.08(2)	0.35 ± 0.15	2.48	0.08(2)	0.09 ± 0.16
Sr	38	2.87	–	–	–	3.08	0.19(2)	0.60 ± 0.16	2.82	0.05(2)	0.08 ± 0.15
Y	39	2.21	1.25	0.21(5)	−0.35 ± 0.16	2.43	0.13(9)	0.61 ± 0.14	1.88	0.25(5)	−0.20 ± 0.17
Zr	40	2.58	2.28	0.04(4)	0.31 ± 0.12	3.15	0.12(3)	0.96 ± 0.14	2.67	0.11(6)	0.22 ± 0.13
Nb	41	1.46	–	–	–	1.98	0.06(4)	0.95 ± 0.15	–	–	–
Ba	56	2.18	1.50	0.14(2)	−0.07 ± 0.10	2.73	0.05(3)	0.94 ± 0.05	2.00	0.10(2)	−0.05 ± 0.07
La	57	1.10	0.85	0.14(7)	0.36 ± 0.11	1.45	0.07(9)	0.74 ± 0.10	1.16	0.16(10)	0.19 ± 0.11
Ce	58	1.58	1.12	0.11(5)	0.15 ± 0.07	1.84	0.09(8)	0.65 ± 0.07	1.53	0.05(4)	0.08 ± 0.06

			TYC 3305−571−1			TYC 3423−6966−1			TYC 4684−2242−1		
	Z	$\log_\odot\epsilon^a$	$\log\epsilon$	σ_l(N)	[X/Fe] ± σ_t	$\log\epsilon$	σ_l(N)	[X/Fe] ± σ_t	$\log\epsilon$	σ_l(N)	[X/Fe] ± σ_t
C	6	8.43	8.30	0.10(4)	−0.08 ± 0.11	8.60	0.10(3)	0.15 ± 0.12	8.40	0.10(4)	0.02 ± 0.11
N	7	7.83	8.30	0.10(10)	0.52 ± 0.07	8.30	0.15(15)	0.45 ± 0.06	8.50	0.06(15)	0.72 ± 0.05
O	8	8.69	8.90	0.10(1)	0.29 ± 0.13	8.90	0.10(1)	0.22 ± 0.12	8.90	0.10(1)	0.26 ± 0.12
Na	11	6.24	6.53	0.08(2)	0.34 ± 0.12	6.60	0.10(2)	0.34 ± 0.13	6.60	0.10(2)	0.41 ± 0.13
Mg	12	7.60	–	–	–	–	–	–	8.20:	0.10(1)	0.65 ± 0.15
Rb	37	2.52	2.55	0.10(2)	0.08 ± 0.16	2.80	0.10(2)	0.26 ± 0.16	2.60	0.10(1)	0.13 ± 0.17
Sr	38	2.87	3.05	0.10(2)	0.25 ± 0.12	3.34	0.06(2)	0.45 ± 0.10	2.58	0.28(2)	−0.24 ± 0.22
Y	39	2.21	2.18	0.14(8)	0.02 ± 0.14	2.36	0.19(7)	0.13 ± 0.15	2.04	0.14(8)	−0.12 ± 0.14
Zr	40	2.58	2.78	0.02(3)	0.25 ± 0.12	2.80	0.10(3)	0.20 ± 0.14	2.75	0.05(4)	0.22 ± 0.12
Nb	41	1.46	–	–	–	–	–	–	1.80:	0.10(1)	0.39 ± 0.15
Ba	56	2.18	2.50	0.10(2)	0.37 ± 0.08	2.20	0.10(1)	0.00 ± 0.11	2.20	0.10(2)	0.07 ± 0.07
La	57	1.10	1.53	0.04(8)	0.48 ± 0.10	1.27	0.12(5)	0.15 ± 0.11	1.26	0.04(5)	0.21 ± 0.10
Ce	58	1.58	1.88	0.15(5)	0.35 ± 0.10	1.77	0.05(3)	0.02 ± 0.06	1.67	0.11(6)	0.14 ± 0.07

			TYC 4837−925−1			TYC 591−1090−1			TYC 752−1944−1		
	Z	$\log_\odot\epsilon^a$	$\log\epsilon$	σ_l (N)	[X/Fe] ± σ_t	$\log\epsilon$	σ_l(N)	[X/Fe] ± σ_t	$\log\epsilon$	σ_l(N)	[X/Fe] ± σ_t
C	6	8.43	8.00	0.10(4)	−0.16 ± 0.11	8.40	0.10(4)	0.27 ± 0.11	8.35	0.05(4)	0.00 ± 0.10
N	7	7.83	8.00	0.10(15)	0.44 ± 0.06	8.15	0.15(15)	0.47 ± 0.07	8.45	0.05(15)	0.70 ± 0.05
O	8	8.69	8.60	0.10(1)	0.18 ± 0.12	8.40	0.20(2)	0.01 ± 0.16	8.75	0.10(1)	0.17 ± 0.12
Na	11	6.24	6.25	0.05(2)	0.28 ± 0.11	6.05	0.05(2)	0.11 ± 0.11	6.45	0.10(2)	0.28 ± 0.13
Mg	12	7.60	–	–	–	–	–	–	7.75	0.15(2)	0.23 ± 0.15
Rb	37	2.52	–	–	–	–	–	–	2.80	0.10(1)	0.28 ± 0.17
Sr	38	2.87	2.79	0.18(2)	0.19 ± 0.16	2.80	0.10(1)	0.23 ± 0.13	3.09	0.18(1)	0.30 ± 0.12
Y	39	2.21	1.74	0.12(6)	−0.20 ± 0.14	3.03	0.04(9)	1.12 ± 0.13	2.60	0.10(5)	0.47 ± 0.14
Zr	40	2.58	2.48	0.02(3)	0.17 ± 0.16	3.37	0.07(5)	1.09 ± 0.12	3.09	0.02(4)	0.59 ± 0.12
Ba	56	2.18	2.00	0.10(2)	0.09 ± 0.07	3.00	0.15(2)	1.12 ± 0.11	2.70	0.10(1)	0.60 ± 0.10
La	57	1.10	1.08	0.04(6)	0.25 ± 0.09	1.95	0.14(8)	1.15 ± 0.11	1.59	0.11(5)	0.57 ± 0.11
Ce	58	1.58	1.50	0.10(5)	0.19 ± 0.07	2.36	0.16(4)	1.08 ± 0.10	2.03	0.06(7)	0.53 ± 0.06

[a]Asplund et al. (2009)
: Uncertain abundances due to a noisy or blended region